Check for updates

ADVANCED ENGINEERING MATERIALS
www.aem-journal.com

A Simulative Approach for the Prediction of Mesoscale Residual Stress Fields in Solution-Strengthened Ferritic Ductile Iron

Lutz Horbach, Oliver Schenk, Valérian Iss, Ali Rajaei, Jiali Zhang, Felix Weber, and Christoph Broeckmann*

Ductile cast iron (DCI) is characterized by excellent mechanical properties, good castability, and low cost. This predestines it for use in large structural components. However, its highly heterogeneous microstructure and the associated thermal expansion mismatch between graphite and matrix, as well as the phase transformation that occurs during cooling to ambient temperature, result in a highly complex residual stress state in the DCI microstructure. These residual stresses are of non-negligible magnitude and have a significant impact on the resulting macroscopic mechanical properties of DCI. Experimental measurement of the mesoscopic residual stress fields is complex and equipment is limited, so reliable models for numerical prediction are increasingly in focus. Herein, a representative volume element-based simulation approach is presented that can be used to predict the mesoscopic residual stress and strain fields in the DCI microstructure. The applicability of a Johnson–Mehl–Avrami–Kolmogorov model, extended for continuous cooling rates, to predict transformation kinetics is demonstrated. The model is calibrated for a silicon solid solution-strengthened DCI alloy and various cooling rates. The resulting stresses and strains are calculated and the effect of cooling rate variation on the mesoscopic residual stress and strain fields is discussed.

1. Introduction

The growing demand for renewable energy has led to a continuous requirement on weight reduction and size increase of the wind turbines (WT), which are subject to increasingly loads.[1] Ductile cast iron (DCI) as a widely used structural material in this field offers a unique combination of excellent mechanical properties, good castability, and low costs.[2,3] Its microstructure, consisting of spheroidal graphite precipitates that are embedded in a ferritic and/or pearlitic matrix, allows mechanical properties to be tailored over a wide range by adjusting the matrix composition.[4,5] Besides these advantages, the silicon solid solution-strengthened DCI (SSF-DI) grades exhibit enhanced mechanical properties compared to conventional DCI grades. Different studies have shown that increasing silicon content up to 4.3 wt% leads to improvements in yield strength, tensile strength, and hardness.[6–8] In addition, silicon increases the austenite–ferrite transformation temperature in DCI, which favors the formation of ferrite over pearlite by allowing more time for austenite to transform to ferrite.[9] This can effectively stabilize the mechanical properties by eliminating the cementite lamellae.

Despite the increasing demand for WT components, operational failures remain rare, reflecting the high safety potential of these systems.[10] However, the conservative safety factors used in modern WT components hinder economically efficient and sustainable design strategies, as oversized designs are often employed to compensate for uncertainties and variations in local mechanical properties.[11] Here, the variations of local mechanical properties must be considered on a global and a local scale. Global property variation is associated with a variation of local solidification and cooling conditions, as often found especially in heavy-section castings. Local property variation is caused by the inherent uncertainty of cast materials due to several effects, such as the heterogeneity of the DCI microstructure and the superimposed influence of microshrinkage or porosity.[11,12] Addressing these factors in future design strategies can greatly improve their efficiency and lead to significant material savings. Weber et al.[11] presented a multidomain optimization approach for ADI-GJS-1050-6 that incorporated local microstructure-dependent fatigue strength into the topology optimization of a WT planet carrier, resulting in a 17% weight reduction. Although this concept considered local fatigue strengths, the influence of residual stresses was not considered. However, cast structural

L. Horbach, O. Schenk, V. Iss, A. Rajaei, J. Zhang, F. Weber, C. Broeckmann
Institute for Materials Applications in Mechanical Engineering (IWM)
RWTH Aachen University
52062 Aachen, Germany
E-mail: l.horbach@iwm.rwth-aachen.de

The ORCID identification number(s) for the author(s) of this article can be found under https://doi.org/10.1002/adem.202500326.

© 2025 The Author(s). Advanced Engineering Materials published by Wiley-VCH GmbH. This is an open access article under the terms of the Creative Commons Attribution License, which permits use, distribution and reproduction in any medium, provided the original work is properly cited.

DOI: 10.1002/adem.202500326

components inherently exhibit significant first- and second-order process-induced residual stresses caused by the thermal gradients during solidification and cooling.[13,14] As DCI components are frequently subjected to cyclic loading in a variety of applications,[15,16] the superposition of these residual stresses with the external cyclic loads results in a complex, highly multiaxial and nonproportional stress state, which requires careful consideration in the design process to ensure structural integrity and performance.

The formation of residual stresses of second order in DCI is highly dependent on the microstructure and consequently on process conditions such as cooling rate. The residual stresses develop essentially during cooling to ambient temperature due to mismatches in thermal expansion coefficients between graphite and the surrounding matrix, as well as due to phase transitions.[17,18] Research indicates that second-order residual stresses reach maximum at the interface between graphite precipitates and the matrix, so that dislocation plasticity of the matrix can be triggered.[19,20] Zhang et al. reported that such stresses in ferritic DCI grades can be even as high as the half of the macroscopic yield strength of the matrix at room temperature.[17] These localized stress concentrations, which act as microstructural notches, often serve as primary crack initiation sites in the absence of casting defects such as microshrinkage or porosity.[21,22] Experimental techniques such as synchrotron X-ray diffraction (XRD) provide valuable insight into second order residual stress distributions, but are costly and limited in accessibility.[23–25]

An alternative to the highly complex and often destructive experimental residual stress identification methods is the model-based analysis and prediction, e.g., by finite element analysis. Reliable numerical models allow for prediction and analysis of residual stress fields under varying process conditions, which enables their integration into structural design. To the best knowledge of the authors, only one model developed by Andriollo et al.[26] which incorporates the austenite–ferrite phase transition in a simplified manner, exists for the numerical prediction of second order residual stresses. The model accounts for the difference in thermal expansion coefficients of austenite and ferrite while neglecting the effect of the phase transition kinetics, transformation strains, and transformation plastic strains. On the other hand, although Andriollo et al.[26] have made extensive efforts to realistically model the graphite phase, including its highly complex inhomogeneous internal structure based on a variety of conical sectors and orientations, their work is limited to modeling of a single graphite precipitates and its surrounding matrix. Crucial factors such as the interaction of stress fields between neighboring graphite precipitates have not been considered in the model. As a result, while the model is capable of analyzing various influencing factors on the residual stress field of a single graphite precipitate, it cannot effectively predict the effect of second-order residual stresses on the mechanical properties of DCI.

Recent modeling approaches based on representative volume elements (RVEs) of the DCI microstructure offer a promising extension in this area and the ability to consider the effect of interacting stress and strain fields surrounding neighboring graphite precipitates. However, due to the complexity of the DCI microstructure, the constitutive behavior of both the graphite and matrix phases is typically modeled as homogeneous and isotropic, with constitutive equations being mostly empirical in nature.[27–29] In contrast, crystal plasticity (CP) models based on a multiplicative decomposition of the deformation gradient allow the consideration of the underlying physical mechanisms and constitutive equations capable of describing the behavior of single crystals by linking the stress and strain tensor.[30] Two different types of CP models can be distinguished. Dislocation based models, which allow the consideration of physical quantities such as dislocation densities, and phenomenological models, which have been established as an efficient way to model the deformation behavior of polycrystalline microstructures.[30] CP models have been often used for steels.[31] However, the computational effort and the complexity of parameter determination increase significantly with the complexity of the model.[32,33] Consequently, only a few studies have applied CP-based models to simulate the deformation behavior of the highly heterogeneous DCI microstructure.[32,34] The authors themselves employed a phenomenological CP model to analyze the effect of silicon microsegregation on the macroscopic mechanical properties of an equivalent DCI grade, a process that involved considerable effort in parameter determination.[32]

This study presents an RVE-based simulation approach for predicting process-related residual stresses in SSF-DI at a mesoscale. The RVE-based approach allows to capture the effect of interacting stress and strain fields of neighboring graphite precipitates, which is a significant improvement over existing models. The finite element model evaluates the coupled thermomechanical and metallurgical mechanisms during cooling from casting to ambient temperature. The phase transformation kinetics are modeled using a differential formulation of the Johnson–Mehl–Avrami–Kolmogorov (JMAK) equation. Calibrated by dilatometry experiments for various cooling rates, this model accurately captures the effect of varying cooling rates of fully solidified SSF-DI and explicitly accounts for the influence of cooling conditions on phase transformations. The constitutive deformation behavior of the matrix phase is modeled as orthotropically elastic and perfectly plastic, taking into account the crystallographic orientations of individual grains in the elastic properties and the temperature dependence of all required model parameters. Thus, the presented model provides an efficient tool for predicting second order residual stress fields and helps to reduce the uncertainties in predicting the local mechanical properties of SSF-DI, thereby enabling the full potential of the material to be exploited.

2. Experimental Section

2.1. Material

The SSF-DI alloy investigated in this study has been the subject of previous studies and publications. The interested reader is referred to these studies for more detailed information on the production of the material.[8,35] All castings were done in Y2 standard test blocks (geometric module: 10 mm) according to DIN EN 1563-04.[36] The chemical composition of the SSF-DI alloy investigated is given in **Table 1**, where the carbon equivalent (CEV) is determined according to

© 2025 The Author(s). Advanced Engineering Materials published by Wiley-VCH GmbH

15272648, 0, Downloaded from https://advanced.onlinelibrary.wiley.com/doi/10.1002/adem.202500326 by Rwth Aachen University Zentraler Rechnungseingang, Wiley Online Library on [19/05/2025]. See the Terms and Conditions (https://onlinelibrary.wiley.com/terms-and-conditions) on Wiley Online Library for rules of use; OA articles are governed by the applicable Creative Commons License

Table 1. Chemical compositions measured by optical emission spectroscopy and the corresponding CEVs of the investigated material.

C [wt%]	Si [wt%]	P [wt%]	Mn [wt%]	Mg [wt%]	Fe [wt%]	CEV [wt%]
3.25	3.52	0.03	0.12	0.05	92.7	4.43

$$\mathrm{CEV} = \mathrm{C}\,[\mathrm{wt\%}] + \frac{\mathrm{Si}\,[\mathrm{wt\%}] + \mathrm{P}\,[\mathrm{wt\%}]}{3} \quad (1)$$

In addition to the SSF-DI alloy, whose chemical composition is given in Table 1, a pure ferritic steel was cast in Y2 standard test blocks. This material, hereafter referred to as the equivalent matrix material, has the same chemical composition as the matrix of the SSF-DI alloy investigated at room temperature and is used to determine the yield strength of the ferritic SSF-DI matrix as a function of temperature, as outlined later. It should be noted that the carbon concentration of the SSF-DI matrix changes during heating and cooling due to carbon diffusion out of and into the graphite, which could not be accounted for by the equivalent matrix. However, given that the effect of varying carbon content would dramatically increase the cost of material casting, specimen preparation, and experimental testing, this simplification represents a valid compromise.

2.2. Experimental Methods

2.2.1. Optical Microscopy

The microstructure of all specimens was first characterized by optical microscopy (OM). Metallographic specimens were taken from the geometric center of each cast block, and then ground and polished according to standard metallographic preparation procedures. To analyze the size distribution, volume fraction, and morphology of the graphite precipitates, ten optical micrographs were taken from each unetched specimen using a Zeiss Axio Imager M2m optical microscope. This renders a total analyzed area of $14.17 \times 10.62\,\mathrm{mm}^2$ (captured area of $1.417 \times 1.062\,\mu\mathrm{m}^2$ for each optical micrograph) for each material state, which ensure sufficient statistics. According to DIN EN ISO 945-4,[37] a minimum of 500 graphite precipitates were captured and analyzed to determine their diameter, nodularity, and density. Nodularity, defined as the percentage of spheroidal graphite, was evaluated according to ASTM E2567.[38] In order to characterize the matrix composition of the material, samples were etched with 2% nitric acid for 2 min.

2.2.2. Scanning Electron Microscopy

Scanning electron microscopy (SEM) analyses were performed using a FEI Helios Nanolab G3 CX DualBeam system (Thermofisher GmbH, Dreieich, Germany) equipped with an EDAX/TSL system (AMETEK GmbH, Weiterstadt, Germany) with a Hikari camera for electron backscatter diffraction (EBSD) and an Octane detector for energy-dispersive spectroscopy measurements. EBSD was used to characterize the ferrite grain size distribution of each sample. Large-area EBSD scans covering $1000 \times 1000\,\mu\mathrm{m}^2$ were performed at an accelerating voltage of 20 kV and a beam current of 11 nA with a step size of 1 μm, providing sufficient statistical data for the determination of the ferrite grain size distribution.

2.2.3. Macroscopic Tensile Tests and Hardness Measurements

To characterize the mechanical properties under monotonic loading, macroscopic uniaxial tensile tests and Brinell hardness measurements were performed. For each material, tensile specimens of type B with a diameter of 10 mm were prepared according to DIN 50125.[39] The strain rate controlled tensile tests were performed under quasistatic conditions with a strain rate of $0.002\,\mathrm{s}^{-1}$ to obtain the ultimate tensile strength (UTS), the 0.2% offset yield strength ($\sigma_{Y0.2}$), and elongation at fracture (A). Brinell hardness was determined according to DIN EN ISO 6506[40] with a ball diameter of 2.5 mm and a load of 1839 N (187.5 kp).

2.2.4. Dilatometry Experiments

While the model developed in this work aims at the calculation of mesoscale strains and stresses, the macroscopically manifested length changes during cooling are an essential part of both model derivation and validation. These include both the thermal expansion of the material and the transformation strains induced by the phase transformation from austenite to ferrite, which may be superimposed by additional plastic, elastic, and transformation plastic strains. In this work, these length changes were evaluated using the DIL 805 quenching dilatometer from TA Instruments. Cylindrical samples with a diameter of 4 mm and a length of 10 mm were austenitized at 1000 °C, followed by a dwell time of 3 min. The samples were then cooled at various cooling rates as listed in **Table 2**, with the cooling rates maintained constant between 1000 and 500 °C in each experiment. The cooling rates were selected based on preliminary examination in such a way that the additional formation of pearlite in the DCI matrix was prevented. Both heating and cooling were accomplished by induction in high vacuum. The change in length was continuously measured by quartz glass push rods, while the temperature was measured by a thermocouple (type S).

As the yield strength of the ferritic matrix of the SSF-DI material decreases significantly with an increase of temperature, both elastic and plastic strains may occur during cooling. The temperature-dependent yielding behavior of the ferritic matrix was therefore investigated by additional experiments, utilizing the deformation mode of the dilatometer. Cylindrical specimens of the equivalent matrix material with a diameter of 4 mm and a length of 10 mm, having the same chemical composition as the

Table 2. Selected cooling rates of the samples under investigation, with the cooling rate maintained constant between 1000 and 500 °C in each experiment.

Sample	Cooling rate [$\mathrm{K\,s}^{-1}$]
1	0.030
2	0.038
3	0.078
4	0.085

© 2025 The Author(s). Advanced Engineering Materials published by Wiley-VCH GmbH

15272648, 0, Downloaded from https://advanced.onlinelibrary.wiley.com/doi/10.1002/adem.202500326 by Rwth Aachen University Zentraler Rechnungseingang, Wiley Online Library on [19/05/2025]. See the Terms and Conditions (https://onlinelibrary.wiley.com/terms-and-conditions) on Wiley Online Library for rules of use; OA articles are governed by the applicable Creative Commons License

matrix of the tested SSF-DI material, were fabricated and heated to different temperatures ranging from room temperature to 1000 °C at a constant heating rate of 3 K s^{-1}. The temperatures used for testing were 25, 200, 400, 600, 800, and 1000 °C. Subsequently, a uniaxial load was applied at a constant deformation rate of 0.02 mm s^{-1} using compression punches made of quartz glass that were connected to a hydraulic unit allowing for a maximum load of 20 kN. For each temperature, two identical samples were tested. The length change was recorded by push rods being attached to both compression punches. Each force displacement curve was then transformed to a true stress–strain curve. The stress being observed at 0.2% plastic deformation was considered as yield strength.

2.3. Simulative Methods

2.3.1. Generation of 3D RVEs

In order to accurately predict the stress and strain fields, 3D RVEs were generated based on the previously determined microstructural characteristics of samples 1–4. Due to the significant influence of grain orientation on the local stress and strain fields, the individual ferrite grains of the matrix are explicitly modeled and taken into account in the RVE. In the first step, artificial 3D grain structures were created using Neper,[41,42] based on the measured grain size distributions of the individual samples. These artificially generated grain structures were then read using a Python script and reconstructed in Abaqus,[43] where all grains were assembled into a complete grain structure by means of Boolean operations (see step 1 in **Figure 1**). Step 2 involved the generation of graphite precipitates approximated as spheres. These spheres were placed in the RVE using a random sequential absorption algorithm, ensuring that their centers were located at grain triple points. The algorithm was terminated when the target graphite volume fraction was reached. The underlying size distribution of the spheres representing the graphite precipitates was based on their actual spatial distribution. For this purpose, the 2D graphite precipitate size distributions measured from optical micrographs of each sample specimen were converted into 3D spatial distributions using stereological methods.[44,45] In step 3, the graphite precipitates were subtracted from the grain structure to generate the ferritic matrix. In steps 4 and 5, the graphite precipitates and the modeled matrix were combined, followed by trimming of the RVE. Finally, the mesh was generated in step 6.

2.3.2. Model Assumptions, Material Parameters, and Boundary Conditions

The element count of all models was determined by a preliminary convergence study. All interfaces in the models, including grain–grain and grain–graphite interfaces, were assumed to be perfectly bonded. Since the matrix of each sample has no texture, individual grain orientations were randomly assigned. The grains in the ferritic matrix were modeled as orthotropically elastic and isotropically plastic, with their yield strength determined as a function of temperature by dilatometry experiments as described above. The graphite precipitates were modeled as isotropically elastic and perfectly plastic, with temperature-independent behavior. The elastic constants of ferrite[46] and graphite,[47] the yield strength of graphite,[48] and the specific heat, thermal conductivity, and thermal expansion of graphite[49] as well as the thermal conductivity and specific heat of ferrite[50] were obtained from the literature based on the cited references and are given in **Table 3** and **4**. The thermal expansion of ferrite was calculated using the model described below and implemented in the simulation via a user subroutine.

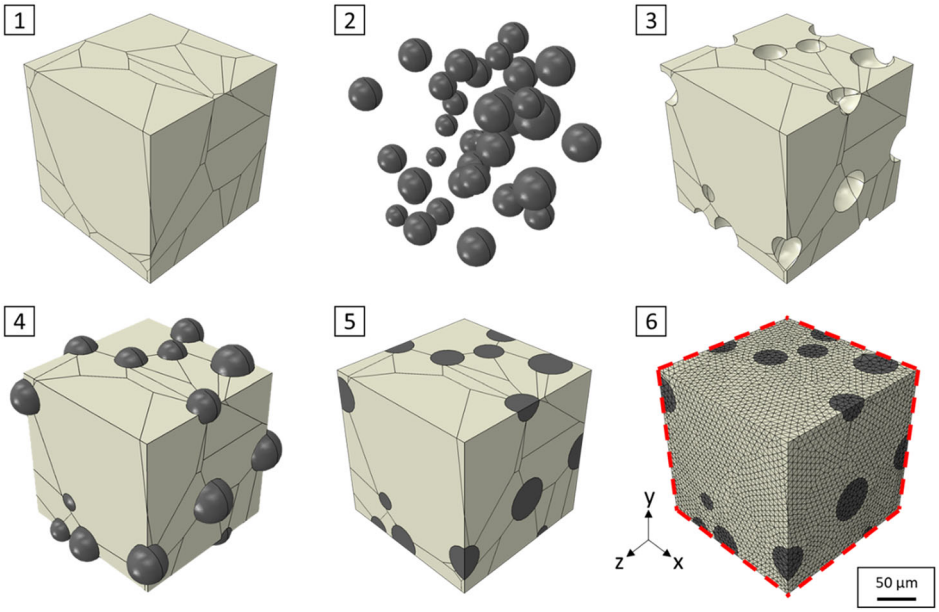


Figure 1. Schematic representation of the RVE generation process in Abaqus.[43] On the red dashed line marked surfaces, the symmetrical boundary conditions are applied as mechanical boundary conditions.

© 2025 The Author(s). Advanced Engineering Materials published by Wiley-VCH GmbH

15272648, 0, Downloaded from https://advanced.onlinelibrary.wiley.com/doi/10.1002/adem.202500326 by Rwth Aachen University Zentraler Rechnungseingang, Wiley Online Library on [19/05/2025]. See the Terms and Conditions (https://onlinelibrary.wiley.com/terms-and-conditions) on Wiley Online Library for rules of use; OA articles are governed by the applicable Creative Commons License

15272648, 0, Downloaded from https://advanced.onlinelibrary.wiley.com/doi/10.1002/adem.202500326 by Rwth Aachen University Zentraler Rechnungseingang, Wiley Online Library on [19/05/2025]. See the Terms and Conditions (https://onlinelibrary.wiley.com/terms-and-conditions) on Wiley Online Library for rules of use; OA articles are governed by the applicable Creative Commons License

Table 3. Thermal conductivity k, specific heat c_p, and elastic constants of the SSF-DI matrix.

Temperature [°C]	k [mW mm^{-1} K^{-1}]	c_p [10^6 mJ ton^{-1} K^{-1}]	c_{11} [10^3 MPa]	c' [10^3 MPa]	c_{44} [10^3 MPa]
0	59.5	–	–	–	–
25	–	–	232.2	48.3	117.0
100	57.8	481	227.7	46.7	115.4
200	53.2	519	221.5	44.1	113.2
300	49.4	553	214.2	41.1	111.1
400	–	595	205.6	38.0	109.1
500	45.6	662	196.8	34.4	107.2
600	36.8	754	186.7	30.1	105.3
700	33.1	867	173.8	24.8	103.1
800	28.5	875	158.1	17.0	100.5
900	–	846	148.8	13.3	99.0
1000	27.6	–	–	–	–

Table 4. Thermal conductivity k, specific heat c_p, coefficient of thermal expansion α, Young's modulus E, Poisson's ratio ν, and yield limit σ_Y of graphite.

Temperature [°C]	k [mW mm^{-1} K^{-1}]	c_p [10^6 mJ ton^{-1} K^{-1}]	α [10^{-6} 1/K]	E [10^3 MPa]	ν [–]	σ_Y [MPa]
0	136.0	–	4.85	25.5	0.312	30
100	125.5	933.15	4.96			
200	115.7	1154.5	5.08			
300	106.6	1341.1	5.19			
400	98.4	1486.8	5.30			
500	90.8	1603.5	5.42			
600	84.1	1697.4	5.53			
700	78.0	1773.6	5.65			
800	72.8	1835.6	5.76			
900	68.3	1886.7	5.88			
1000	64.5	1929.4	5.99			

The generated models were used to simulate the dilatometry experiments. An initial temperature of 1000 °C was applied to all models, resulting in a purely austenitic matrix in each model at the start of the simulation. The cooling rates of all models were adapted from the experimentally set cooling rates in the dilatometry experiments (see Table 2) to accurately model the cooling process. The temperature distribution was assumed to be constant over the RVE domain at each time increment. All simulations were carried out until a final temperature of 20 °C (room temperature) was reached. Symmetrical boundary conditions were applied as mechanical boundary conditions in the x-, y- and z-directions on the surfaces marked by the red dashed lines in Figure 1.

In order to statistically validate the results of the residual stress simulations, three RVEs with an edge length of 150 µm were generated for each of the four samples (1–4) examined by means of the dilatometry experiments, resulting in a total of 12 RVEs, each with different grain and graphite precipitate structures. The resulting strain and stress fields were extracted at each time step for analysis.

2.3.3. Modeling of Austenite to Ferrite Phase Transformation

The simulation of a heat treatment is based on the description of three different fields, which encompass the temperature distribution due to heat conduction, the provoked phase transformations, and the hereby induced strains and stresses. While the temperature distribution results from joule heat conduction, the description of the occurring phase transformations necessitates an appropriate constitutive description. For diffusive phase transformations, as the transformation from austenite to ferrite, the phenomenological JMAK model introduced by Johnson, Mehl, Avrami, and Kolmogorov, has proven to be suitable to replicate the kinetics of the phase transformation. It was initially derived for isothermal phase transformations and describes the amount of a specific phase i as a function of time t, the equilibrium phase amount $\bar{\xi}_i$ that may form at a given temperature T, as well as two phenomenological model parameters n and τ that indicate the transformation rate and the time delay of the transformation, respectively:

$$\xi_i(t) = \bar{\xi}_i \cdot \left[1 - \exp\left\{-\left(\frac{t}{\tau}\right)^n\right\}\right] \tag{2}$$

This model may be adopted to continuous cooling conditions by considering the differential from of Equation (2) and its integration over time. However, notable deviations from experimental results were found with increasing cooling rate $\dot{T}$,[51,52] which is to be taken into account by multiplication with a correction factor $f(\dot{T})$:[53]

$$\dot{\xi}_i = n \cdot \left(\frac{\bar{\xi}_i - \xi_i}{\tau}\right) \cdot \left[\ln\left(\frac{\bar{\xi}_i}{\bar{\xi}_i - \xi_i}\right)\right]^{\frac{n-1}{n}} \cdot f(\dot{T}) \tag{3}$$

2.3.4. Modeling of Strains and Stresses

The computation of the residual stresses is based on the strains occurring in the individual phases during cooling and the hereby induced mismatch. Both graphite and ferrite are subject to thermal expansion ε_{th}. Since austenite is characterized by a higher packing density of the atoms, the phase transformation to ferrite is associated with an elongation that is commonly referred to as transformation strain ε_{tr}. Once subjected to an additional load during this phase transformation, the material may experience additional plastic transformation. This effect, known as transformation plasticity strain ε_{tp}, requires stresses that are significantly lower than the yield strength. These stresses may be either due to external loads or to local strain fields that are induced by gradients of temperature or microstructure. In addition, both elastic and plastic strains ε_{el} and ε_{pl} may occur as well. As each strain

 © 2025 The Author(s). Advanced Engineering Materials published by Wiley-VCH GmbH

component is rather small, their superposition may be calculated by assuming additivity of individual strain increments:

$$\dot{\varepsilon} = \dot{\varepsilon}_{\text{th}} + \dot{\varepsilon}_{\text{tr}} + \dot{\varepsilon}_{\text{tp}} + \dot{\varepsilon}_{\text{el}} + \dot{\varepsilon}_{\text{pl}} \tag{4}$$

The strain increment due to thermal expansion and phase transformations is given by

$$d\varepsilon_{\text{ii,th}} + d\varepsilon_{\text{ii,tr}} = \sum_k (\alpha_k \cdot dT + b_k \cdot d\xi_k) \tag{5}$$

With α_k and b_k being the coefficients of thermal expansion and the transformation strains of the phase k, ξ_k represents the volume fraction of phase k and dT is the temperature increment. To calculate transformation strains, the austenitic microstructure at 1000 °C is used as a reference state, which is assumed to be strain free. With this assumption, the transformation strains represent the intercept of the linear fit of the temperature versus strain curve for a fully homogeneous phase at 20 °C.

The transformation plasticity was incorporated by postulating a linear dependency on the deviatoric stress component S_{ij}:

$$\varepsilon_{ij,\text{tp}} = \frac{3}{2} K_{\text{tp}} \cdot S_{ij} \cdot \xi(2 - \xi) \tag{6}$$

In this work, K_{tp} was assumed to be 5×10^{-5} in correspondence to literature data.[54,55]

The elastic strain ε_{el} and plastic strain ε_{pl} were calculated assuming the elastic and plastic properties of each microstructural constituent modeled as described above.

2.3.5. Model Calibration

A precise description of the phase transformation and the occurring length changes necessitates the knowledge on the model parameters n, τ, $\dot{\xi}_i$ and $f(\dot{T})$ as well as the transformation strain ε_{tr}. Once being applied to homogeneous materials, these model parameters can be derived based on length changes occurring during the phase transformation that directly indicate the phase amount being transformed as well as the associated strain. However, experimental evaluation is complicated by the presence of the graphite precipitates in the microstructure of the material investigated, which neither undergoes phase transformation nor exhibits characteristic transformation strains. Therefore, the model parameters were obtained using an inverse calibration technique as described below.

The results of the dilatometry experiments were used to calibrate the model. The coefficients of thermal expansion of austenite and ferrite were directly determined by calculating the slope of the measured strain versus temperature curves of each sample above and below the austenite–ferrite transformation temperature, respectively. As cooling rates that provoke a full transformation to ferrite are considered only, the equilibrium phase fraction $\dot{\xi}$ is given as 1. The parameter $f(\dot{T})$ was initially set to 1 and the above parameters were first calibrated for sample 1. The dilatometry experiment was simulated using RVE simulations of the generated RVEs and the parameters were adjusted until the simulated strain–temperature curve fits the experimentally measured curve of sample 1. Once appropriate parameters for n, τ, and ε_{tr} were identified, the calibration was continued for the remaining samples to determine the function $f(\dot{T})$ that captures the influence of varying cooling rates on the phase transition kinetics. For remaining samples, the parameters n and τ were assumed to be constant, taking their values from sample 1. Only the function $f(\dot{T})$ and the transformation strain ε_{tr} were iteratively adjusted, for each sample, i.e., for each cooling rate, until the strain–temperature curves of the remaining samples fit their corresponding experimentally measured curves. The transformation strain ε_{tr} is calibrated for each sample as it is expected to have a strong effect on the resulting strain and stress fields.

3. Results and Discussion

3.1. Pristine Microstructure

The pristine microstructure of the samples investigated is characterized by the morphology of the graphite precipitates and the nature of the ferritic matrix, i.e., the matrix composition and the grain size distribution. OM was used to study the graphite phase, while large-area EBSD scans provided statistical information on the grain size distribution of the matrix phase. The results of the graphite precipitate analysis are summarized in **Table 5**. Based on these results, it can be observed that the mean Feret diameter of the graphite precipitates in the as-cast condition is clearly smaller than that of the samples subjected to the dilatometry experiments. In addition, the mean Feret diameter appears to increase slightly with higher cooling rates among the samples examined by dilatometry experiments, although this trend is negligibly small. While the area fraction of the graphite is kept in a relatively constant level, the subtle increase in the size of the graphite precipitates resulted in a reduction of precipitate density. Similarly, the nodularity shows a slight but negligible decrease. However, all samples maintain a relatively high nodularity. **Figure 2** presents selected optical micrographs of the samples at the unetched state, which are used for quantitative graphite analysis. It is necessary to note that Figure 2 can only show a general trend, given the inherent local scatter in graphite size distribution and morphology. Nevertheless, a comparison between the as-cast material and sample 4 shows a significant decrease in graphite nodule density, accompanied by a noticeable increase in average graphite precipitate diameter. **Table 6** shows the average ferrite grain size and the corresponding standard deviation in brackets for all samples. Representative details of the large-area EBSD scans are shown in **Figure 3**. However,

Table 5. Quantitative graphite precipitate analysis.

Sample	Cooling rate [K s^{-1}]	$\overline{D}_{\text{Feret}}$ [µm]	Nodularity [%]	Nodule density [1 mm^{-2}]	Graphite fraction [%]
As-cast	–	23.01	86	272	11.2
1	0.030	26.60	86	234	10.6
2	0.038	29.00	84	220	11.6
3	0.078	29.23	81	216	11.6
4	0.085	29.44	81	197	10.7

© 2025 The Author(s). Advanced Engineering Materials published by Wiley-VCH GmbH

15272648, 0, Downloaded from https://advanced.onlinelibrary.wiley.com/doi/10.1002/adem.202500326 by Rwth Aachen University Zentraler Rechnungseingang, Wiley Online Library on [19/05/2025]. See the Terms and Conditions (https://onlinelibrary.wiley.com/terms-and-conditions) on Wiley Online Library for rules of use; OA articles are governed by the applicable Creative Commons License

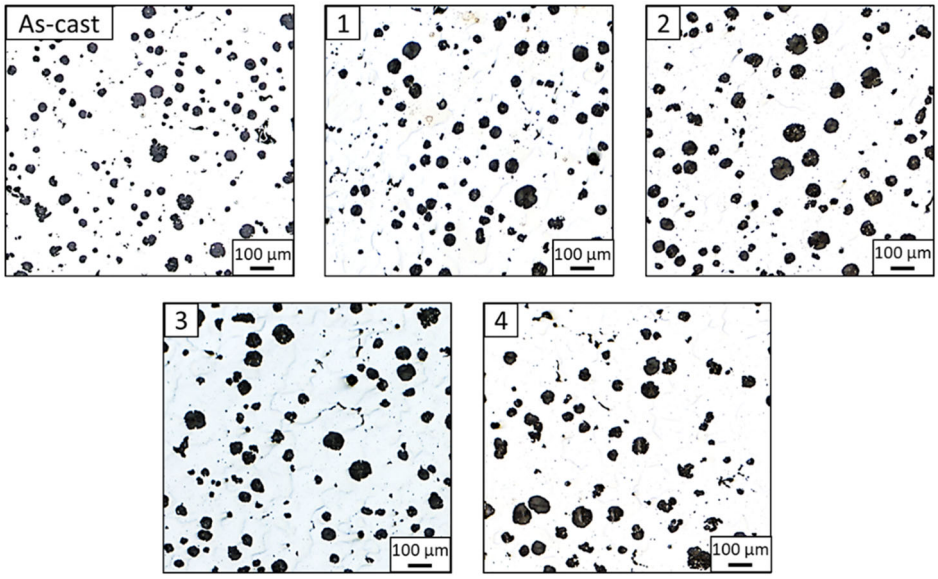


Figure 2. Unetched light microscopy of the different samples for quantitative graphite modulus analysis.

Table 6. Average ferrite grain size determined by large-area EBSD scans and standard deviation.

Sample	Cooling rate [K s^{-1}]	Average ferrite grain size [µm]	St. dev. [µm]
As-cast	–	43.85	21.44
1	0.030	44.76	17.55
2	0.038	47.69	19.72
3	0.078	41.60	16.92
4	0.085	43.04	14.82

neither the grain size data in Table 6 nor the EBSD scans in Figure 3 show a clear trend in grain size variation. In addition, optical micrographs of the samples etched with 2% nitric acid were used to confirm that the matrix of each sample is purely ferritic.

In addition, the mechanical properties under quasistatic loading and the results of the Brinell hardness measurements for the material in the as-cast condition are shown in **Table 7**. Both tensile properties and hardness values were averaged over five specimens or indents, with the corresponding standard deviations shown in parentheses.

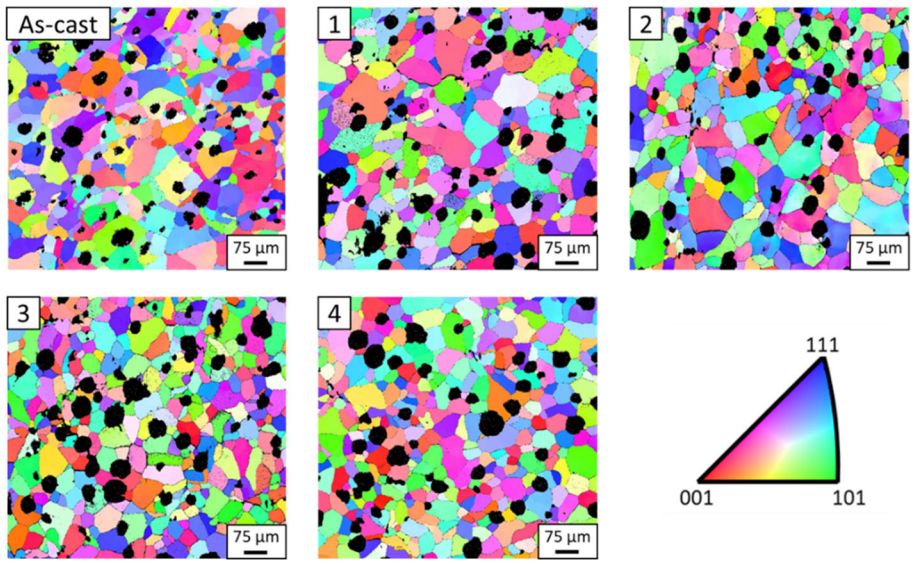


Figure 3. EBSD orientation maps show the comparison of characteristics of matrix ferrite phase of the different samples.

© 2025 The Author(s). Advanced Engineering Materials published by Wiley-VCH GmbH

15272648, 0, Downloaded from https://advanced.onlinelibrary.wiley.com/doi/10.1002/adem.202500326 by Rwth Aachen University Zentraler Rechnungseingang, Wiley Online Library on [19/05/2025]. See the Terms and Conditions (https://onlinelibrary.wiley.com/terms-and-conditions) on Wiley Online Library for rules of use; OA articles are governed by the applicable Creative Commons License

Table 7. Average mechanical properties of the investigated material in the as-cast condition, including yield limit ($\sigma_{Y0.2}$), ultimate tensile strength (UTS), elongation at fracture (A_t), and Brinell hardness ($HBW_{2.5/187.5}$); standard deviation in parentheses.

Block	$\sigma_{Y0.2}$ [MPa]	UTS [MPa]	A_t [%]	$HBW_{2.5/187.5}$
As-cast	408 (3.9)	522 (1.6)	17.3 (0.7)	182.7 (4.6)

Table 8. Inversely calibrated values for the coefficients of thermal expansion α of ferrite and austenite and the JMAK model kinetic parameters n and τ.

$\alpha_{Ferrite}$ [10^{-6} 1/K]	$\alpha_{Austenite}$ [10^{-6} 1/K]	τ [s]	n [–]
13.4	31.9	1640	0.75

3.2. Results of the Dilatometry Experiments and the Model Calibration

The yield strength of the matrix was determined as described above by compression tests performed in the dilatometer at various temperatures as described. **Figure 4** shows the resulting stress–strain curves parameterized by the corresponding testing temperatures. A significant decrease in yield strength with increasing temperature is evident from these curves. In addition, there is a strongly noticeable change in the strain-hardening behavior over varying temperatures. At room temperature, the matrix exhibits significant strain hardening that decreases with temperature, resulting in near-ideal plastic behavior at 1000 °C, with near-zero yield strength. In **Figure 5**, the experimentally determined yield strength values are plotted as a function of temperature, revealing a drastic decrease in yield strength with increasing temperature, following a trend that closely resembles a Boltzmann function.

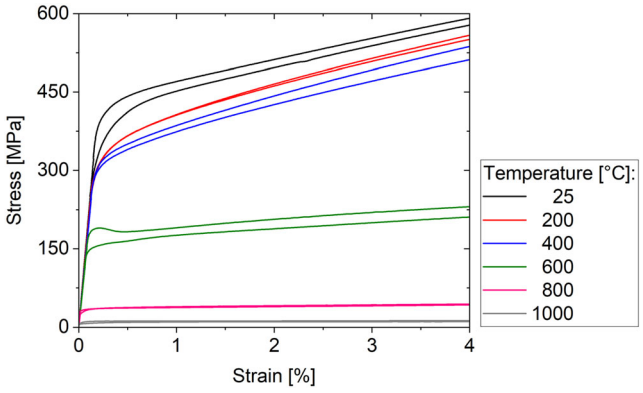


Figure 4. Stress–strain curves derived from compression tests on equivalent matrix material samples, parameterized by testing temperature.

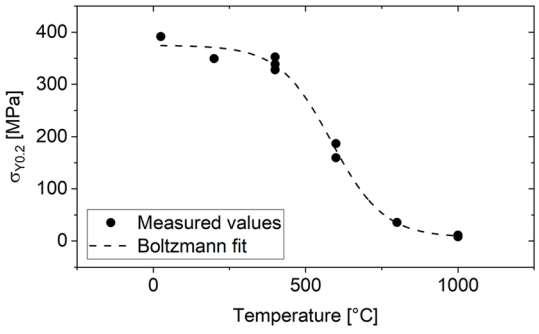


Figure 5. The 0.2% plastic strain offset yield strength determined by compression tests as a function of the testing temperature.

The model calibration was performed as described in Section 2.3.5 and the appropriate values for the kinetic parameters of the JMAK model n and τ were determined (cf., **Table 8**). Subsequently, the transformation strain ε_{tr} and the correction factor $f(\dot{T})$ were determined for all samples, taking into account the different cooling rates. **Figure 6** shows the simulated strain versus temperature curves adjusted by inverse calibration compared to the experimentally measured curves for each sample.

Obviously, there is a strong agreement between the simulated and experimentally measured curves after the inverse calibration of the model. However, the experimentally measured strain–temperature curves shown in Figure 6 vary significantly among the different samples. The leap attributed to the austenite–ferrite phase transition in the curves shows significant differences in both height and width over the different cooling rates, with sample 1 exhibiting the lowest cooling rate and sample 4 the highest. In **Figure 7**, the calibrated values for the transformation strain ε_{tr} and the parameter $f(\dot{T})$ are plotted against the cooling rates of the investigated samples, revealing a clear dependency. The transformation strain decreases with increasing cooling rate, suggesting a potential quadratic relationship between ε_{tr} and cooling rate. Conversely, the parameter $f(\dot{T})$ exhibits an inverse trend, increasing approximately linearly with cooling rate. **Figure 8** shows the austenite and ferrite phase fractions for an RVE of sample 1 (cooling rate: 0.03 K s^{-1}) and an RVE of sample 4 (cooling rate: 0.085 K s^{-1}) as a function of time during the austenite–ferrite phase transformation. The increasing values of the correction factor $f(\dot{T})$ with higher cooling rates accelerate the phase transformation. Consequently, the phase transformation in the RVE of sample 4 takes less than half of the transformation time in the RVE of sample 1.

3.3. Results of the RVE Simulations

The RVE simulations were performed as previously described, with three RVEs simulated per sample, corresponding to each cooling rate. **Figure 9** shows the distribution of equivalent plastic strain at room temperature for a representative RVE from each sample and its corresponding cooling rate. Bands of plastic deformation are evident, particularly at the interfaces between the graphite precipitates and the surrounding matrix. For better visualization, the graphite precipitates have been excluded from the figure. Notably, regions of closely spaced graphite precipitates show extensive zones of plastic deformation. Based on the results shown in Figure 9, no major differences are observed in the distribution of equivalent plastic strain across the RVEs.

Figure 10 shows the normal stresses in the z-direction along with the von Mises equivalent stresses for the same RVEs after

© 2025 The Author(s). Advanced Engineering Materials published by Wiley-VCH GmbH

15272648, 0, Downloaded from https://advanced.onlinelibrary.wiley.com/doi/10.1002/adem.202500326 by Rwth Aachen University Zentraler Rechnungseingang, Wiley Online Library on [19/05/2025]. See the Terms and Conditions (https://onlinelibrary.wiley.com/terms-and-conditions) on Wiley Online Library for rules of use; OA articles are governed by the applicable Creative Commons License

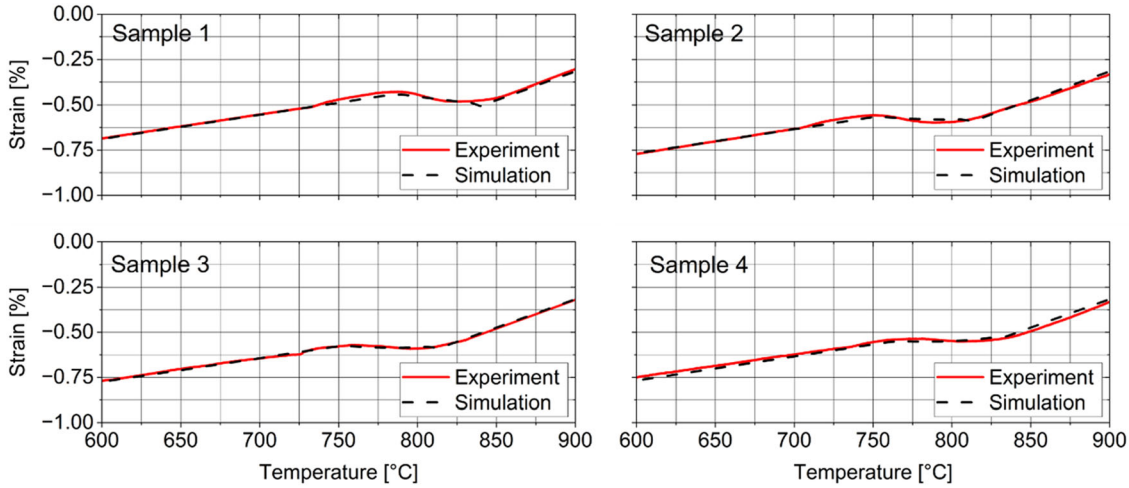


Figure 6. Comparison of simulated and experimentally measured strain versus temperature curves for samples 1–4.

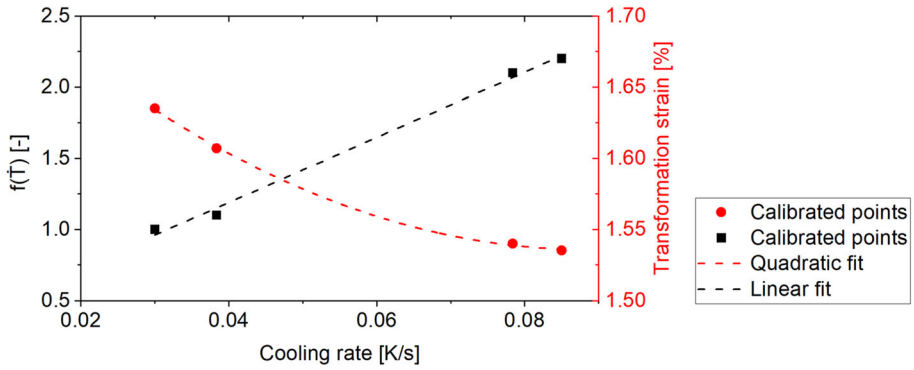


Figure 7. Values of the parameter $f(\dot{T})$ and the transformation strain ε_{tr} determined by the described inverse calibration technique as a function of the cooling rate of the studied samples.

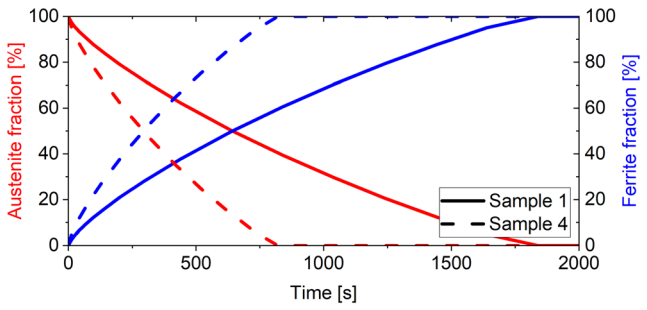


Figure 8. Visualization of the time required for the austenite–ferrite transformation for an RVE of sample 1 compared to an RVE of sample 4.

cooling to room temperature. The normal stress distributions in the z-direction highlight the coexistence of tensile and compressive stresses within the matrix, with magnitudes reaching up to 200 MPa in some regions. These stresses are most pronounced near the graphite–matrix interfaces and extend significantly into the surrounding matrix. Figure 10 further indicates that tensile stresses are generally more pronounced than compressive stresses. Besides the normal stress components in the z-direction, the distributions of von Mises equivalent stresses also reach maximum values at the graphite matrix interface. In addition, the stress fields surrounding individual graphite precipitates appear to overlap for precipitates in close proximity. The von Mises equivalent stress also reaches values up to 200 MPa in some critical regions of the RVE. However, there are no clear differences in the stress distributions among the RVEs corresponding to different specimens or cooling rates.

In order to highlight the role of the phase transformation, **Figure 11** shows the evolution of the equivalent plastic strain averaged over the matrix of an RVE of sample 1, together with the austenite and ferrite phase fractions plotted against temperature during cooling. A pronounced increase in the equivalent plastic strain within the matrix is observed during the phase transformation, which continues until it stabilizes at a constant level at a specific temperature. This temperature coincides closely with the completion of the austenite to ferrite phase transformation.

Furthermore, **Figure 12** shows the normal stress components as well as the von Mises equivalent stress, averaged over the matrix of the same RVE, as a function of temperature during

© 2025 The Author(s). Advanced Engineering Materials published by Wiley-VCH GmbH

15272648, 0, Downloaded from https://advanced.onlinelibrary.wiley.com/doi/10.1002/adem.202500326 by Rwth Aachen University Zentraler Rechnungseingang, Wiley Online Library on [19/05/2025]. See the Terms and Conditions (https://onlinelibrary.wiley.com/terms-and-conditions) on Wiley Online Library for rules of use; OA articles are governed by the applicable Creative Commons License

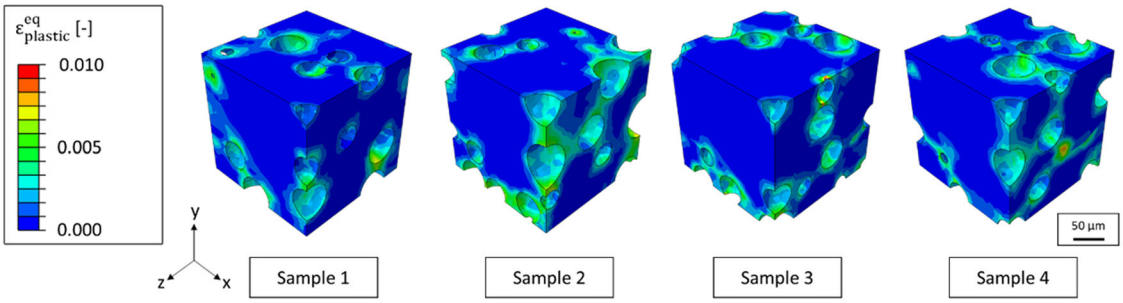


Figure 9. Distribution of equivalent plastic strain at room temperature in the RVE of the investigated samples with corresponding cooling rates, with graphite precipitates omitted for visualization.

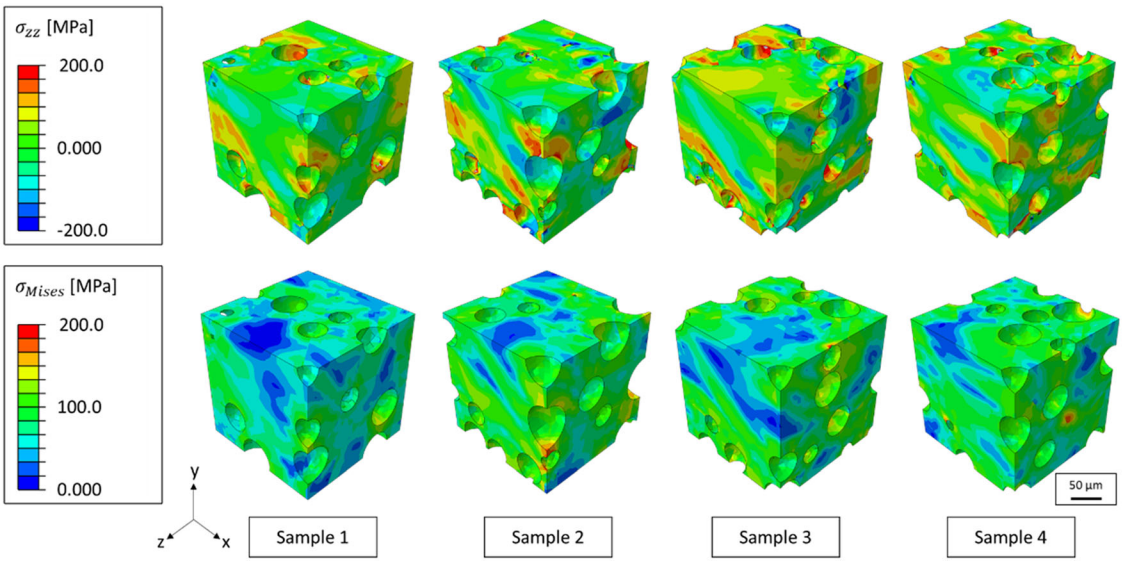


Figure 10. Distribution of stresses in the *z*-direction and von Mises equivalent stresses at room temperature in the RVE of the investigated samples with the corresponding cooling rates, with graphite precipitates omitted for visualization.

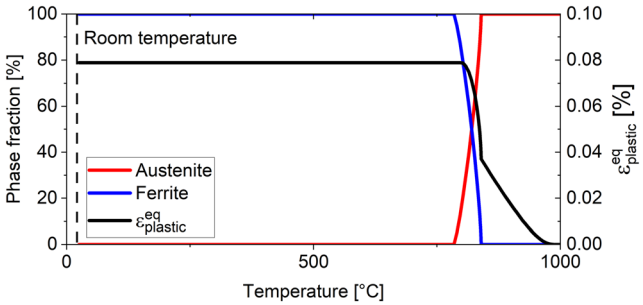


Figure 11. The equivalent plastic strain averaged over the matrix of an RVE of sample 1, together with the austenite and ferrite phase fractions as a function of temperature.

cooling. Initially, all stress components and the von Mises stress show a steady increase until the onset of the phase transformation, at which point a sudden drop in all stresses is observed. After this drop, the von Mises stress increases rapidly, while the normal stress components resume a nearly linear increase after the phase transformation is complete. Unlike the equivalent plastic strain, all stress measures in Figure 12 continue to increase throughout the cooling process.

To assess potential differences between RVEs from different samples or cooling rates, the von Mises equivalent stress and equivalent plastic strain, both averaged over the matrix at room temperature, are used as comparative measures. **Figure 13** shows these metrics for all simulated RVEs as a function of their respective cooling rates. A linear regression line, accompanied by a 95% confidence interval, highlights the trend observed in the simulated data. The results show a slightly increasing trend in both von Mises equivalent stress and equivalent plastic strain with increasing cooling rates, indicating a possible correlation between cooling rate and mechanical response of the matrix.

4. Discussion

The here presented study introduces an RVE simulation-based approach to predict the mesoscopic residual strain and residual stress fields of SSF-DI as a function of cooling rate while

© 2025 The Author(s). Advanced Engineering Materials published by Wiley-VCH GmbH

15272648, 0, Downloaded from https://advanced.onlinelibrary.wiley.com/doi/10.1002/adem.202500326 by Rwth Aachen University Zentraler Rechnungseingang, Wiley Online Library on [19/05/2025]. See the Terms and Conditions (https://onlinelibrary.wiley.com/terms-and-conditions) on Wiley Online Library for rules of use; OA articles are governed by the applicable Creative Commons License

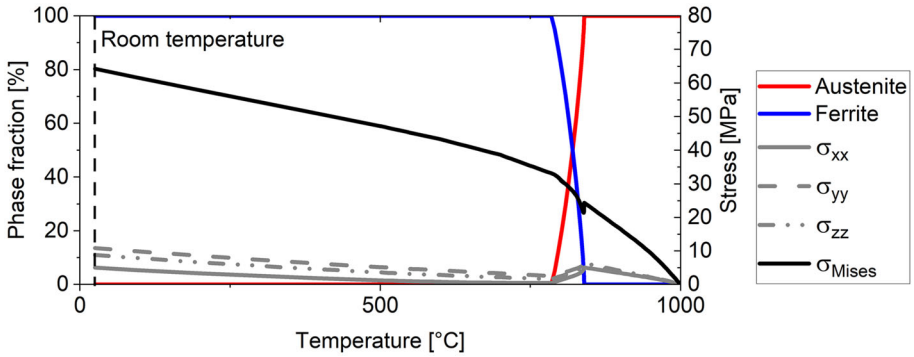


Figure 12. The von Mises equivalent stress and the normal stress components averaged over the matrix of an RVE of sample 1, together with the austenite and ferrite phase fractions as a function of temperature.

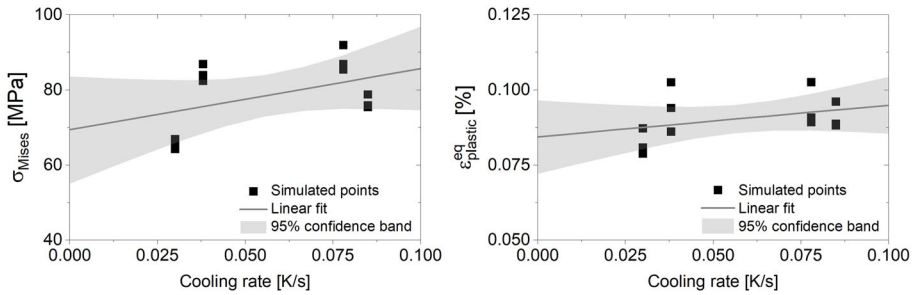


Figure 13. The equivalent von Mises stress and equivalent plastic strain averaged over the ferrite matrix of all RVEs plotted as a function of cooling rate.

accounting for the austenite-to-ferrite phase transformation. The model employed describes the phase transformation kinetics using an JMAK model augmented with a correction factor $f(\dot{T})$ to account for the dependency of the cooling rates. The material and model parameters used are partly based on literature values. Parameters describing the phase transformation kinetics, the transformation strains and the transformation plasticity, as well as the rate-dependent correction factor $f(\dot{T})$, and the coefficients of thermal expansion of austenite and ferrite were determined by means of dilatometry experiments. In the following, the results are systematically discussed.

4.1. Pristine Microstructure

The pristine microstructure of the samples studied is characterized by a slight coarsening of the average graphite precipitate size and, conversely, a decrease in nodule density compared to the as-cast material. With increasing temperature, the solubility of carbon in the matrix of the samples increases significantly due to the austenitization process. Consequently, carbon diffuses from the graphite precipitates into the face-centered-cubic (fcc) austenite lattice, resulting in partial dissolution of smaller graphite precipitates. Upon subsequent cooling to room temperature, the austenite becomes supersaturated and carbon solubility in the matrix decreases again, resulting in graphite reformation. The precipitated graphite attaches to the existing graphite precipitates, which serve as nucleation sites, resulting in coarsening of the graphite precipitates. This phenomenon is commonly observed during the heat treatment of DCI.[56,57] However, the size distribution of the graphite precipitates is mainly dominated by the heterogeneous nucleation during solidification and the degree of undercooling at the eutectic transition, which is significantly controlled by the local cooling rate.[58–60] Compared to these influencing factors, the coarsening of the graphite precipitates due to carbon diffusion during the austenitization in the dilatometer plays a minor role, which explains the only slight differences in the average graphite precipitate size between the investigated samples. In cast components, however, the difference is expected to be more pronounced due to the difference in nucleation and cooling during eutectic transformation. Since graphite precipitate size significantly affects residual stresses in DCI, it is important to consider the graphite morphology and size distribution that develops under real casting conditions when evaluating component performance.[17,18] Due to the relatively small differences in the cooling rates of the dilatometer samples, the variations in the average graphite precipitate diameter among the samples 1–4 in Table 5 can be attributed to statistical scatter.

Similarly, the resulted ferrite grain size is primarily influenced by the nucleation phase and subsequent grain growth, with nucleation typically occurring homogeneously at the austenite grain boundaries, making the austenite grain size a dominant influencing factor on the resulting ferrite grain size.[61–63] All samples investigated were austenitized in the dilatometer under identical conditions, suggesting that the austenite grain size after

© 2025 The Author(s). Advanced Engineering Materials published by Wiley-VCH GmbH

15272648, 0, Downloaded from https://advanced.onlinelibrary.wiley.com/doi/10.1002/adem.202500326 by Rwth Aachen University Zentraler Rechnungseingang, Wiley Online Library on [19/05/2025]. See the Terms and Conditions (https://onlinelibrary.wiley.com/terms-and-conditions) on Wiley Online Library for rules of use; OA articles are governed by the applicable Creative Commons License

austenitization is expected to be comparable for all samples.[64] Due to the relatively small differences in the cooling rates studied, no significant grain growth was observed in the samples analyzed.

4.2. Dilatometry Experiments and Model Calibration

Several studies have shown that the modified JMAK model can accurately predict diffusive phase transitions such as the austenite–ferrite transformation.[53,65,66] The strong agreement between simulated and experimentally measured strain–temperature curves at different cooling rates in this work further confirms its applicability to nonisothermal phase transformations during continuous cooling.

The values of the correction factor $f(\dot{T})$ obtained by inverse calibration show an increase with increasing cooling rates, indicating accelerated austenite–ferrite phase transformation kinetics, which is in agreement with previous findings. Bharadwaj et al.[67] investigated the effect of cooling rate on the phase transformation kinetics and microstructure of Nb–Ti microalloyed low-carbon high-strength low-alloy steel and attributed the accelerated phase transformation kinetics to increased undercooling of the austenite at higher cooling rates.[67] Consequently, the driving force for phase transformation increases with cooling rate.

Furthermore, the calibrated values for the transformation strain ε_{tr} tend to decrease with increasing cooling rates. As explained previously, ε_{tr} results from the different atomic packing densities of the body-centered cubic ferrite lattice and the face-centered cubic (fcc) austenite lattice. For a constant chemical composition, implying constant lattice parameters for both ferrite and austenite, ε_{tr} should be independent of cooling rate. However, the observed cooling rate dependency of ε_{tr}, as shown in Figure 7, can be attributed to several factors. On the one hand, SSF-DI shows a highly heterogeneous microstructure consisting of graphite precipitates embedded in an iron matrix acting as carbon sources. Austenite and ferrite both show decreasing carbon solubility with decreasing temperature. As more carbon is dissolved in the fcc austenite lattice, its lattice parameter increases, resulting in a more pronounced difference in lattice parameter between austenite and ferrite due to phase transformation. Rapid cooling causes greater undercooling so that the austenite–ferrite transformation is initiated at lower temperatures where less carbon is dissolved in the austenite lattice and the austenite consequently has a smaller lattice parameter. As a result, the transformation strain ε_{tr} decreases with increasing cooling rate.

On the other hand, differences in cooling rate also affect the transformation plastic strain ε_{tp}. Unlike ε_{tr}, ε_{tp} occurs in homogeneous materials only under the influence of external loading during the phase transformation. According to Greenwood and Johnson,[68] ε_{tp} occurs during diffusive phase transformations due to strain accommodation caused by volume differences between the two phases. Although the SSF-DI dilatometry specimens were tested in the absence of external loading, the graphite precipitates present in the microstructure impose an internal load on the surrounding matrix material due to the difference in thermal expansion, leading to a transformation plastic strain in the matrix during the transformation.

The formulation of ε_{tp} as a linear function of the deviatoric part of the stress tensor used in this work is based on the mathematical model of Leblond.[54,55] The linearity through the constant K_{tp} implies that the transformation plastic strain is independent of the cooling rate, which has also been assumed here for simplicity. However, it has previously been shown that ε_{tp} is indeed a function of cooling rate, with increasing transformation plastic strains at decreasing cooling rates.[69] The onset of the austenitic–ferrite phase transformation is shifted to higher temperatures as the cooling rate decreases, resulting in a lower yield point of the matrix material, leading to an earlier onset of plastic deformation.[69] Conversely, faster cooling results in greater undercooling, leading to a lower onset temperature of the phase transition at which the yield strength of the matrix material is higher, limiting plastic deformation.[69]

As mentioned above, the yield strength of the DCI matrix was determined by compression tests at different temperatures using an equivalent matrix material with the same chemical composition as the DCI matrix but without free carbon. A similar approach was previously used by Andriollo et al.[26] However, the absence of the graphite phase introduces a limitation that will be discussed in the following. The ferrite-stabilizing effect of silicon[70,71] suppresses the ferrite–austenite phase transformation in the equivalent matrix material in the absence of graphite. Consequently, the measured yield strength underestimates the true yield strength of SSF-DI at temperatures above the phase transformation because the higher carbon concentration in austenite enhances solid solution strengthening. However, the strengthening effect of interstitial carbon is relatively small,[72] as is the resulting difference in predicted residual stress fields. Given the considerable experimental effort required to determine yield strength at different carbon contents, this limitation represents a reasonable compromise between accuracy and feasibility.

4.3. RVE Simulations

The results of the RVE simulations performed in this work, shown in Figure 9 and 10, indicate that the interface between the graphite precipitates and the ferrite matrix is most critical region, regardless of the cooling rate considered. A plastically deformed region forms around the graphite precipitates near the interface in the matrix. Notably, the size of the plastically deformed region varies with the nodule density. Figure 11 shows the matrix-averaged equivalent plastic strain of the RVE as a function of temperature, combined with the austenite and ferrite phase fractions to visualize the temperature interval at which the phase transformation occurs. The increase in plastic strain during phase transformation can be explained by the transformation strain ε_{tr} and the transformation plastic strain ε_{tp}. In addition, at high temperatures, the yield strength of the SSF-DI matrix is sufficiently low that the matrix allows plastic deformation at relatively low stress levels, which explains the significant accumulation of plastic strain at high temperatures. The subsequent increase in yield strength with decreasing temperature leads to a stagnation of plastic deformation once the temperature falls below a certain temperature at which the stresses are no

 © 2025 The Author(s). Advanced Engineering Materials published by Wiley-VCH GmbH

15272648, 0, Downloaded from https://advanced.onlinelibrary.wiley.com/doi/10.1002/adem.202500326 by Rwth Aachen University Zentraler Rechnungseingang, Wiley Online Library on [19/05/2025]. See the Terms and Conditions (https://onlinelibrary.wiley.com/terms-and-conditions) on Wiley Online Library for rules of use; OA articles are governed by the applicable Creative Commons License

15272648, 0, Downloaded from https://advanced.onlinelibrary.wiley.com/doi/10.1002/adem.202500326 by Rwth Aachen University Zentraler Rechnungseingang, Wiley Online Library on [19/05/2025]. See the Terms and Conditions (https://onlinelibrary.wiley.com/terms-and-conditions) on Wiley Online Library for rules of use; OA articles are governed by the applicable Creative Commons License

longer high enough to exceed the yield limit of the matrix (cf., Figure 11).

Furthermore, when considering the stress distributions shown in Figure 10, it is crucial to note that neither the magnitude of the von Mises equivalent stress nor the magnitude of the stress tensor components is of negligible order. Thus, it is obvious that the residual stresses due to cooling are important to consider in the design of structural components. Both the magnitude of the stress components and the von Mises equivalent stress reach values up to 200 MPa in regions close to the graphite–matrix interface, which corresponds to about 50% of the matrix yield limit and is therefore in close agreement with the results of Zhang et al.[17] The maximum stresses occur at the matrix–graphite interface and decrease with increasing distance from the interface, which also confirms the results found in the literature.[14,17,18] However, from the results it is evident that the stress fields surrounding individual precipitates overlap and interact, emphasizing that the consideration of a single graphite precipitate is definitely not sufficient to investigate the effect of second-order residual stresses on the effective material properties of SSF-DI. Therefore, an RVE of the microstructure must be considered to capture the complex interaction of individual stress fields.

Based on the results shown in Figure 13, differences in the kinetics of the austenitic–ferrite phase transition affect both the residual stress field and the plastic strains induced by cooling. As mentioned above, none of the dilatometry samples examined showed significant differences in graphite precipitate size distribution, allowing the conclusion that the increase in matrix averaged stresses and plastic strains with increasing cooling rate is primarily due to the change in either the phase transformation kinetics or the transformation and plastic strains with varying cooling rate. Zhang et al.[17] also observed a slight increase in residual stresses, ≈5–8%, with higher cooling rates as determined by synchrotron XRD measurements. In addition, the size of the graphite precipitate diameter has been shown to affect the magnitude and distribution of the surrounding residual stresses.[14,17,18,26] The stress gradient in the matrix orthogonal to the interface of stresses in the radial direction, normalized to the graphite precipitate diameter, was found to be identical for graphite precipitates of different sizes, indicating that the depth of penetration of residual stresses into the matrix scales with the graphite precipitate diameter.[26] Therefore, it is critical to consider the true graphite precipitate diameter distribution when evaluating second order residual stresses, as this directly affects the assessment of effective material properties.

A potential future improvement of the model could be a more accurate representation of the highly complex graphite–matrix interface in the DCI microstructure. In the present study, the interface was modeled as perfectly bonded, could be a strong restriction under certain loading conditions. Existing studies have shown that, depending on the strength of the matrix, debonding of the graphite–matrix interface is one of the dominant damage mechanisms in DCI under the influence of external tensile loading conditions.[73–75] However, Andriollo et al.[26] demonstrated that the assumption of a perfectly bonded graphite–matrix interface in the absence of external loading, only for the simulation of the cooling process to ambient temperature, does not lead to significant differences in the predicted residual stress fields since mainly normal compressive stresses are transmitted across the interface during cooling. Nevertheless, the consideration of potential debonding effects remains relevant, especially if the model is to be used in the future to predict the resulting mechanical properties.

Based on the results of the present study, it can be concluded that the consideration of process-induced residual stresses is essential for an accurate simulation-based prediction of the macroscopic mechanical properties of DCI. In particular, regions of pronounced tensile stress around graphite precipitates are critical under cyclic loading because they serve as crack initiation sites in the absence of casting defects such as shrinkage pores, as mentioned earlier. However, the extent to which these residual stresses can be influenced or even controlled requires further investigation. In addition to the altered phase transformation kinetics, the microstructure of DCI also varies with different cooling conditions. Both factors have been shown to strongly influence the resulting residual stress fields, highlighting the need for sophisticated studies to fully understand these complex interactions.

5. Conclusions

The present study introduces an RVE-based approach for the numerical prediction of mesoscopic residual strain and stress fields in SSF-DI. The austenite–ferrite transformation kinetics were modeled using a modified JMAK model extended for different continuous cooling conditions. The model was calibrated for four different cooling rates based on results from dilatometry experiments. Based on the results, the following conclusions can be drawn. The modified JMAK model, including the correction factor $f(\dot{T})$ adjusted for different cooling rates, accurately describes the kinetics of the diffusive austenite-ferrite transformation in the SSF-DI matrix. Both the transformation strain ε_{tr} and the transformation plastic strain ε_{tp} exhibit a cooling rate dependency which affects the resulting strain and stress distributions at room temperature. This rate dependency must be taken into account in order to accurately predict the residual stress distribution based on local cooling conditions. As the cooling rate increases, both plastic strain and residual stress increase in the SSF-DI matrix. Since the dilatometry specimens do not show a significant difference in their graphite precipitate size distributions, the observed effect is mainly attributed to the altered phase transformation kinetics and rate dependency of ε_{tr} and ε_{tp}. The effect of different cooling rates on the size distribution of graphite precipitates cannot be fully investigated using dilatometry experiments, as nucleation and eutectic transformation significantly affect the resulting size distribution. Since the residual stress fields of neighboring graphite precipitates overlap and interact, detailed modeling of a representative volume of the microstructure is required to accurately assess the influence of second order residual stresses on the resulting mechanical properties of SSF-DI.

Acknowledgements

The authors acknowledge funding by the Deutsche Forschungsgemeinschaft (DFG, German Research Foundation) within the project "Experimentell gestützte Modellierung der Korrelation zwischen

 © 2025 The Author(s). Advanced Engineering Materials published by Wiley-VCH GmbH

metallurgischer Prozessführung, 3D-Gefügeentwicklung und mechanischen Eigenschaften von perlitischem Gusseisen mit Kugelgraphit" under grant no. 504974025.

Open Access funding enabled and organized by Projekt DEAL.

Conflict of Interest

The authors declare no conflict of interest.

Author Contributions

Lutz Horbach: investigation (lead); methodology (lead); software (lead); writing—original draft (lead). **Oliver Schenk**: investigation (supporting); methodology (supporting); software (supporting); writing—original draft (supporting). **Valérian Iss**: investigation (supporting); methodology (supporting); software (supporting); writing—review & editing (equal). **Ali Rajaei**: investigation (supporting); methodology (supporting); software (supporting); writing—review & editing (equal). **Jiali Zhang**: supervision (supporting); writing—review & editing (equal). **Felix Weber**: supervision (supporting); writing—review & editing (equal). **Christoph Broeckmann**: funding acquisition (lead); supervision (supporting); writing—review & editing (equal).

Data Availability Statement

The data that support the findings of this study are available from the corresponding author upon reasonable request.

Keywords

ductile cast iron, microstructures, process–structure–property–performance, representative volume elements, residual stress prediction

Received: January 31, 2025
Revised: March 18, 2025
Published online:

[1] BWE, Entwicklung von Größe und Durchmesser von Windenergieanlagen in Deutschland in den Jahren 2013 bis 2023 (in Metern) **2024**.
[2] C. Labrecque, *Can. Metall. Q.* **1998**, *37*, 343.
[3] H. Rafsanjani, J. Sørensen, *Energies* **2015**, *8*, 2908.
[4] R. A. Gonzaga, *Mater. Sci. Eng., A* **2013**, *567*, 1.
[5] C. Ripplinger, M. Gastens, J. Zimmermann, B. Pustal, C. Broeckmann, K.-U. Schröder, A. Bührig-Polaczek, *Materials* **2021**, *14*, 2411.
[6] A. Alhussein, M. Risbet, A. Bastien, J. P. Chobaut, D. Balloy, J. Favergeon, *Mater. Sci. Eng. A* **2014**, *605*, 222.
[7] C. Gebhardt, T. Sedlatschek, A. Bezold, C. Broeckmann, *Mech. Mater.* **2021**, *162*, 104056.
[8] L. Horbach, J. Zhang, T. Sedlatschek, F. Weber, C. Gebhardt, B. David Joseph, A. Bührig-Polaczek, C. Broeckmann, *Mater. Des.* **2024**, *244*, 113130.
[9] N. S. Tiedje, *Mater. Sci. Technol.* **2010**, *26*, 505.
[10] Enser Versicherungskontor GmbH, *EVK-Schadensstatistik: Schadensstatistik zu Windenergieanlagen 2010-2015*, Enser Versicherungskontor GmbH, Ense-Oberense, Germany **2018**.
[11] F. Weber, C. Broeckmann, V. Züch, G. Jacobs, J. Zimmermann, K.-U. Schröder, Y. Bami, J. Jakumeit, M. Bodenburg, R. Weiß, *Forsch. Ingenieurwes.* **2023**, *87*, 39.
[12] K. Mukherjee, S. Fæster, N. Hansen, A. B. Dahl, C. Gundlach, J. O. Frandsen, A. Sturlason, *Mater. Charact.* **2017**, *129*, 169.
[13] T. Andriollo, Y. Zhang, S. Fæster, J. Thorborg, J. Hattel, *J. Mech. Phys. Solids* **2019**, *125*, 714.
[14] S. Zhang, Y. Ran, A. Murphy, G. Zhang, W. Wang, *Mater. Manuf. Processes* **2020**, *35*, 1781.
[15] S. Sujakhu, S. Castagne, M. Sakaguchi, K. A. Kasvayee, E. Ghassemali, A. Jarfors, W. Wang, *Fatigue Fract. Eng. Mater. Struct.* **2018**, *41*, 625.
[16] C. Guillemer-Neel, V. Bobet, M. Clavel, *Mater. Sci. Eng., A* **1999**, *272*, 431.
[17] Y. B. Zhang, T. Andriollo, S. Fæster, R. Barabash, R. Xu, N. Tiedje, J. Thorborg, J. Hattel, D. J. Jensen, N. Hansen, *Acta Mater.* **2019**, *167*, 221.
[18] Y. B. Zhang, T. Andriollo, S. Fæster, W. Liu, J. Hattel, R. I. Barabash, *Acta Mater.* **2016**, *121*, 173.
[19] R. J. Arsenault, N. Shi, *Mater. Sci. Eng.* **1986**, *81*, 175.
[20] C. Y. Barlow, N. Hansen, *Acta Metall. Mater.* **1991**, *39*, 1971.
[21] C. Gebhardt, J. Zhang, A. Bezold, C. Broeckmann, *Int. J. Fatigue* **2023**, *168*, 107402.
[22] V. Di Cocco, F. Iacoviello, A. Rossi, M. Cavallini, S. Natali, *Fatigue Fract. Eng. Mater. Struct.* **2013**, *36*, 893.
[23] B. C. Larson, L. E. Levine, *J. Appl. Crystallogr.* **2013**, *46*, 153.
[24] B. C. Larson, W. Yang, G. E. Ice, J. D. Budai, J. Z. Tischler, *Nature* **2002**, *415*, 887.
[25] L. E. Levine, B. C. Larson, W. Yang, M. E. Kassner, J. Z. Tischler, M. A. Delos-Reyes, R. J. Fields, W. Liu, *Nat. Mater.* **2006**, *5*, 619.
[26] T. Andriollo, K. Hellström, M. R. Sonne, J. Thorborg, N. Tiedje, J. Hattel, *J. Mech. Phys. Solids* **2018**, *111*, 333.
[27] L. Collini, A. Pirondi, *Procedia Struct. Integrity* **2019**, *24*, 324.
[28] C. Gebhardt, F. Weber, T. Sedlatschek, A. Bezold, C. Broeckmann, *Fatigue Strength Prediction of Nodular Cast Iron by Shakedown Analysis* **2023**, Vol. *101*, Springer, Cham. pp. 133–158.
[29] X. Luo, T. Andriollo, K. P. Baxevanakis, V. V. Silberschmidt, *Eng. Fail. Anal.* **2025**, *174*, 109459.
[30] F. Roters, M. Diehl, P. Shanthraj, P. Eisenlohr, C. Reuber, S. L. Wong, T. Maiti, A. Ebrahimi, T. Hochrainer, H.-O. Fabritius, S. Nikolav, M. Friak, N. Fujita, N. Grilli, K. G. F. Janssens, N. Jia, P. J. J. Kok, D. Ma, E. Werner, M. Stricker, D. Weygand, D. Raabe, *Comput. Mater. Sci.* **2019**, *158*, 420.
[31] H. J. Bong, H. Lim, M.-G. Lee, D. T. Fullwood, E. R. Homer, R. H. Wagoner, *Mater. Sci. Eng., A* **2017**, *695*, 101.
[32] L. Horbach, C. Gebhardt, J. Zhang, B. D. Joseph, A. Bührig-Polaczek, C. Broeckmann, *Heliyon* **2024**, *10*, e23904.
[33] W. Liu, J. Lian, N. Aravas, S. Münstermann, *Int. J. Plast.* **2020**, *126*, 102614.
[34] V. Balobanov, M. Lindroos, T. Andersson, A. Laukkanen, *Crystals* **2022**, *12*, 238.
[35] L. Horbach, C. Gebhardt, J. Zhang, B. D. Joseph, A. Bührig-Polaczek, C. Broeckmann, *Heliyon* **2024**, *10*, e23904.
[36] DIN EN 1563:2019-04, *Gießereiwesen_- Gusseisen mit Kugelgraphit; Deutsche Fassung EN_1563:2018*. DIN Media GmbH, Berlin **2019**, https://doi.org/10.31030/2792445.
[37] DIN EN ISO 945-1:2019-10, *Mikrostruktur von Gusseisen_- Teil_1: Graphitklassifizierung durch visuelle Auswertung (ISO_945-1:2019); Deutsche Fassung EN_ISO_945-1:2019*, DIN Media GmbH, Berlin **2019**, https://doi.org/10.31030/3091837.
[38] E04 Committee, *Analysis*, ASTM International, West Conshohocken, PA **2023** https://doi.org/10.1520/E2567-16A.
[39] DIN 50125:2016-12, *Prüfung metallischer Werkstoffe_- Zugproben*, Beuth Verlag GmbH, Berlin **2016** https://doi.org/10.31030/2577390.
[40] DIN EN ISO 6506-1:2015-02, *Metallische Werkstoffe_- Härteprüfung nach Brinell_- Teil_1: Prüfverfahren (ISO_6506-1:2014); Deutsche*

© 2025 The Author(s). Advanced Engineering Materials published by Wiley-VCH GmbH

15272648, 0, Downloaded from https://advanced.onlinelibrary.wiley.com/doi/10.1002/adem.202500326 by Rwth Aachen University Zentraler Rechnungseingang, Wiley Online Library on [19/05/2025]. See the Terms and Conditions (https://onlinelibrary.wiley.com/terms-and-conditions) on Wiley Online Library for rules of use; OA articles are governed by the applicable Creative Commons License

Fassung EN_ISO_6506-1:2014, DIN Media GmbH, Berlin **2015** https://doi.org/10.31030/2146324.
[41] R. Quey, P. R. Dawson, F. Barbe, Large-Scale 3D Random Polycrystals for the Finite Element Method: Generation, Meshing and Remeshing.
[42] R. Quey, M. Kasemer, The Neper/FEPX Project: Free / Open-source Polycrystal Generation, Deformation Simulation, and Post-Processing.
[43] M. Smith, *ABAQUS/Standard User's Manual, Version 6.9*, Dassault Systemes Simulia Corp, Providence Rhode Island USA **2009**.
[44] E. R. Weibel, *Int. Rev. Cytol.* **1969**, *26*, 235.
[45] E. R. Weibel, H. Elias, *Introduction to Stereologic Principles*, Springer, Berlin Heidelberg **1967** pp. 89–98.
[46] D. J. Dever, *J. Appl. Phys.* **1972**, *43*, 3293.
[47] J. R. Cost, K. R. Janowski, R. C. Rossi, *Philos. Mag.* **1968**, *17*, 851.
[48] S. Yoda, M. Eto, T. Oku, *J. Nucl. Mater.* **1983**, *119*, 278.
[49] W. D. Swank, F. I. Valentin, M. Kawaji, D. M. McEligot, *Nucl. Technol.* **2017**, *199*, 103.
[50] ASM International (ed.), *Properties and Selection: Irons, Steels, and High-Performance Alloys*, 10th ed., American Society for Metals, Metals Park, OH **1990**.
[51] J. W. Cahn, *Acta Metall.* **1956**, *4*, 572.
[52] M. Lusk, H.-J. Jou, *Metall. Mater. Trans. A* **1997**, *28*, 287.
[53] T. Hart-Rawung, J. Buhl, A. Horn, M. Bambach, M. Merklein, *J. Mater. Process. Technol.* **2023**, *313*, 117856.
[54] J. B. Leblond, *Int. J. Plast.* **1989**, *5*, 573.
[55] J. B. Leblond, J. Devaux, J. C. Devaux, *Int. J. Plast.* **1989**, *5*, 551.
[56] R. B. Gundlach, *Int. J. Metalcast.* **2020**, *14*, 1065.
[57] L. Michels, A. J. F. Pires, C. A. S. Ribeiro, B. Kroka, E. G. Hoel, E. Ott, C. Hartung, *Metall. Mater. Trans. B* **2022**, *53*, 836.
[58] B. Bauer, I. Mihalic Pokopec, M. Petrič, P. Mrvar, *Int. J. Metalcast.* **2020**, *14*, 809.
[59] M. Górny, M. Kawalec, B. Gracz, M. Tupaj, *Metals* **2021**, *11*, 1634.
[60] H. M. Muhmond, H. Fredriksson, *Mater. Sci. Forum* **2018**, *925*, 45.
[61] M. Avrami, *J. Chem. Phys.* **1940**, *8*, 212.
[62] M. Avrami, *J. Chem. Phys.* **1939**, *7*, 1103.
[63] M. Umemoto, Z. Hai Guo, I. Tamura, *Mater. Sci. Technol.* **1987**, *3*, 249.
[64] C. Wang, X. Wang, J. Kang, G. Yuan, G. Wang, *Materials* **2019**, *12*, 1070.
[65] M. Jung, M. Kang, Y.-K. Lee, *Acta Mater.* **2012**, *60*, 525.
[66] S. Kamamoto, T. Nishimori, S. Kinoshita, *Mater. Sci. Technol.* **1985**, *1*, 798.
[67] R. Bharadwaj, A. Sarkar, B. Rakshe, *Metallogr., Microstruct., Anal.* **2022**, *11*, 661.
[68] G. W. Greenwood, R. H. Johnson, *Proc. R. Soc. London, Ser. A* **1965**, *283*, 403.
[69] T. Otsuka, N. Legrand, *ISIJ Int.* **2020**, *60*, 721.
[70] R. González-Martínez, U de La Torre, J. Lacaze, J. Sertucha, *Mater. Sci. Eng., A* **2018**, *712*, 794.
[71] R. González-Martínez, U de La Torre, A. Ebel, J. Lacaze, J. Sertucha, *Mater. Sci. Eng., A* **2018**, *712*, 803.
[72] S. Takeuchi, *J. Phys. Soc. Jpn.* **1969**, *27*, 929.
[73] V. Di Cocco, F. Iacoviello, M. Cavallini, *Eng. Fract. Mech.* **2010**, *77*, 2016.
[74] C. Gebhardt, J. Zhang, A. Bezold, C. Broeckmann, *Int. J. Fatigue* **2023**, *168*, 107402.
[75] G. Hütter, L. Zybell, M. Kuna, *Eng. Fract. Mech.* **2015**, *144*, 118.

© 2025 The Author(s). Advanced Engineering Materials published by Wiley-VCH GmbH

15272648, 0, Downloaded from https://advanced.onlinelibrary.wiley.com/doi/10.1002/adem.202500326 by Rwth Aachen University Zentraler Rechnungseingang, Wiley Online Library on [19/05/2025]. See the Terms and Conditions (https://onlinelibrary.wiley.com/terms-and-conditions) on Wiley Online Library for rules of use; OA articles are governed by the applicable Creative Commons License